Nanomedicine: Nanotechnology, Biology, and Medicine 70 (2025) 102872

Contents lists available at ScienceDirect

Nanomedicine: Nanotechnology, Biology, and Medicine

journal homepage: www.sciencedirect.com/journal/nanomedicine-nanotechnology-biology-and-medicine

Original Article

3D correlative light and electron microscopy reveals the uptake and processing of inorganic-organic hybrid nanoparticles into cancer cells

Louisa Herbsleb [a], David Wild [a], Henriette Gröger [b], Tim Schubert [c], Anna Maria Steyer [d], Julian Hennies [d], Frauke Alves [e,f], Claus Feldmann [b], Andreas Walter [a,*]

[a] Aalen University, Center for Optical Technologies, Anton-Huber-Straße 21, 73430, Aalen, Germany
[b] Institute of Inorganic Chemistry, Karlsruhe Institute of Technology (KIT), Engesserstr. 15, 76131, Karlsruhe, Germany
[c] Aalen University, Materials Research Institute Aalen, Beethovenstr. 1, 73430, Aalen, Germany
[d] EMBL Imaging Centre, European Molecular Biology Laboratory, 69117, Heidelberg, Germany
[e] Translational Molecular Imaging, Max-Planck-Institute for Multidisciplinary Sciences, 37075, Göttingen, Germany
[f] Department for Haematology and Medical Oncology, Department of Clinical and Interventional Radiology, University Medical Center Göttingen, 37075, Göttingen, Germany

ARTICLE INFO

Keywords:
Correlative light and electron microscopy (CLEM)
Inorganic-organic nanoparticles (IOH-NP)
Intracellular uptake and trafficking
Focused ion beam scanning electron microscopy (FIBSEM)
Quantitative confocal fluorescence microscopy

ABSTRACT

Inorganic–organic hybrid nanoparticles (IOH-NPs) are a promising drug delivery system in oncology due to their high drug-load capacity. In this study, we established a 3D correlative light and electron microscopy (CLEM) workflow that combines confocal fluorescence microscopy (FM) with focused ion beam scanning electron microscopy (FIBSEM) to unambiguously identify and visualize the (sub)cellular uptake and processing of reference fluorescently labeled and zirconium-based IOH-NPs in murine H8N8 breast cancer cells. The 3D-CLEM workflow was set up without the need to add external fiducial markers since image correlation was achieved using lipid droplets as intrinsic correlative landmarks. We observed that all H8N8 breast cancer cells had taken up IOH-NPs after 4 h, and most IOH-NPs were found in clusters within the H8N8 cells. IOH-NPs were internalized by endocytosis within 2 h with increasing cellular concentrations over time and accumulated in endolysosomal vesicles over 24 h, while the overall endolysosomal volume increased between 2 and 6 h after IOH-NP incubation and returned to its original value thereafter, remaining stable for up to 48 h. The 3D-CLEM workflow also revealed changes in the morphology and density of the IOH-NPs inside endolysosomal vesicles, suggesting the dissolution of IOH-NPs after 2 h. We also observed mitochondrial swelling in IOH-NP exposed cells, suggesting stress responses even without drug load. The 3D-CLEM workflow provides new insights into the cellular tracking and processing of IOH-NPs and supports the development of novel nanomedicine strategies.

Introduction

By establishing an advanced correlative light and electron microscopy workflow in 3D (3D-CLEM), we visualized and quantified the uptake, cellular distribution and processing of inorganic-organic hybrid nanoparticles (IOH-NPs) in H8N8 murine breast cancer cells. The 3D-CLEM workflow allowed us to unambiguously identify IOH-NPs within their ultrastructural context within entire cancer cells in 3D without the addition of external fiducial markers for correlation. We instead relied on inherent lipid droplets for the alignment between the light and electron microscopy channels. The IOH-NPs can be loaded with one or two chemotherapeutics and represent a promising approach for cancer therapy that has the potential for drug delivery to the tumor site, minimizes side effects and enhance therapeutic efficacy to improve patient care and increase survival rates for cancer patients. The IOH-NPs have been described in detail elsewhere.[1–4]

Inorganic-organic hybrid IOH-NPs (IOH-NPs)

The concept of IOH-NPs was developed for combined therapy and diagnostics, ensuring the highest possible drug loading (>60 % of the nanoparticle (NP) mass) while maintaining a simple chemical composition and straightforward synthesis in water. IOH-NPs are characterized by a saline composition consisting of an inorganic cation and a drug

* Corresponding author.
E-mail address: andreas.walter@hs-aalen.de (A. Walter).

https://doi.org/10.1016/j.nano.2025.102872
Received in revised form 3 September 2025;
Available online 22 October 2025
1549-9634/© 2025 The Authors. Published by Elsevier Inc. This is an open access article under the CC BY license (http://creativecommons.org/licenses/by/4.0/).

anion. The drug anion is functionalized with phosphate, sulfonate, or carboxylate groups. In combination with a suitable cation, these drug anions form poorly soluble compounds in water (e.g., $[ZrO]^{2-}$[5′-fluoro-2′-deoxyuridine-5′-monophosphate, (FdUMP)]$^{2-}$, $[ZrO]^{2+}$[gemcitabine monophosphate (GMP)]$^{2-}$) with 75 wt% FdUMP (chemotherapeutic agent)[1] and 76 wt% GMP (chemotherapeutic agent).[2] Both are examples of chemotherapeutic drug anions. The experiments presented here were conducted with reference IOH-NPs (Ref-IOH-NPs) without an active chemotherapeutic agent to prevent premature cell death and to visualize the effects of the IOH-NPs on cells and their pathways without inducing apoptosis.

Previously, IOH-NPs have been characterized extensively.[3] Detailed analyses confirmed their colloidal stability in water and high drug-load efficiency and were shown to accumulate in an orthotopic pancreatic ductal adenocarcinoma mouse model not only in the primary tumor but also to metastatic sites.[2] The incorporation of the fluorescent dye DUT647 into the IOH-NPs enabled direct visualization of their intracellular distribution using optical imaging.[2] In in vitro studies, the intracellular uptake of IOH-NPs that consist of a cocktail of chemotherapeutic and cytostatic drugs was confirmed, and the synergistic anticancer effect of these IOH-NPs was shown in a murine breast cancer cell line (pH8N8) and a human pancreatic cancer cell line (AsPC1).[3] In AsPC1 cells, DUT647-labeled gemcitabine-free Ref-IOH-NPs turned out to end up in LysoTracker-positive late endosomes and lysosomes.[2] Here, we complement these studies by the 3D visualization of the uptake, subcellular distribution and degradation of zirconium-based and fluorescently labeled IOH-NPs within the ultrastructural context of single cancer cells using an advanced 3D-CLEM workflow.

3D correlative light and electron microscopy (CLEM)

In CLEM, fluorescence microscopy (FM) visualizes the distribution of fluorescently labeled molecules but lacks the information about surrounding structures. This ultrastructural context can be visualized using electron microscopy (EM), which, in turn, lacks high molecular specificity. Only the combination of FM and EM can gather spatial and temporal information about a specific molecule within its subcellular architecture.

The field of CLEM has been receiving more and more attention in the last years and has become the method of choice to target rare processes within cells. However, CLEM often focuses on thin sections of only a few nanometers[5] and lacks robust solutions to re-identify regions of interest (ROIs) after the relocation between imaging platforms.[6–8] In line with similar endeavors,[9] we here add the third dimension to the CLEM-workflow by combining confocal microscopy with focused ion beam scanning electron microscopy (FIBSEM) as a stand-alone imaging technique and work towards automated correlation without the addition of additional fiducial markers. While transmission electron microscopy (TEM) requires thin samples of only about 100 nm in thickness,[10] unprecedented large volumetric reconstructions, such as of entire cells, are now routinely achieved using FIBSEM by sequentially milling and imaging the surface of the sample.[11] The data can then be reconstructed in 3D and provide a comprehensive and accurate view on the subcellular organization of cells and tissues, at a resolution in the nanometer range. To streamline the workflow, we applied a 3D-CLEM approach that enables the unambiguous identification of IOH-NPs without the need to add external fiducial markers, such as fluorescent microspheres (e.g., TetraSpeck™ beads) or quantum dots that are commonly used to register FM and EM images.[12,13] By eliminating external markers, we simplify sample preparation, reduce clustering artefacts, and improve the preservation of the cellular ultrastructure. Instead of these external markers, we rely on endogenous organelles that are electron-dense and can be fluorescently labeled. Specifically, we used lipid droplets stained with BODIPY, which makes them visible in FM, while their high lipid content ensures contrast in EM. These droplets, ranging from 100 to 1000 nm in diameter, served as intrinsic landmarks for the alignment of the 3D-CLEM datasets.[14] The unambiguous localization of IOH-NPs was additionally ensured by their DUT647 fluorophores and the presence of zirconium in the IOH-NPs and its strong electron absorbance, indicative for the localization of IOH-NPs, since zirconium is absent in cells.

3D-CLEM for visualization of nanoparticles in cancer cells

NP uptake in cultured cancer cells primarily occurs via endocytic pathways, resulting in rapid enclosure of particles in early endosomes, followed by trafficking to late endosomes and lysosomes within minutes to hours.[15,16] FM techniques, often employing fluorescently labeled NPs or organelle-specific dyes, have been widely used to monitor uptake dynamics and subcellular colocalization. However, their spatial resolution is limited by diffraction (~200–300 nm), and interpretation can be confounded by the need for specific labeling.[17,18] To overcome these drawbacks in the study of NP, CLEM was employed, and several CLEM studies have localized gold or quantum dot NPs within endolysosomal structures, employing combinations of FM and 2D EM.[19,20] Additionally, cryogenic correlative microscopy combining widefield 3D fluorescence with soft X-ray tomography has been applied to investigate the lysosomal localization of drug-loaded lipid-based nanocarriers.[21] Up to date, CLEM has been applied several times to examine different parts of cells or biological pathways,[14,22,23] as well as using lipid droplets as internal fiducial markers.[14] However, most studies rely on partial or 2D correlation, and true 3D-CLEM workflows that integrate 3D FM with 3D EM (e.g., FIBSEM) for studying the subcellular distribution of drug-delivery-relevant NPs remain very limited. Importantly, to the best of our knowledge, no prior study has applied 3D-CLEM to analyze the subcellular fate of metal-based NPs for drug delivery. Our 3D-CLEM approach allows precise co-localization of fluorescent signals with electron-dense NP structures and their surrounding subcellular compartments in 3D. It overcomes the limitations of conventional 2D EM and diffraction-limited FM by providing an unambiguous ultrastructural context for fluorescent signals across entire cell volumes. The workflow hence represents a significant advancement for nanoscale drug delivery studies. It provides, to the best of our knowledge, for the first time, a 3D correlation of metal-based drug-delivery nanoparticles with their cellular environment at nanometer precision.

Methods

Cell culture of H8N8 cells

Murine H8N8 cells, a basal-like breast cancer cell line with tumor stem cell characteristics derived from bi-transgenic WAP-T/WAP-mutp53 tumors,[24] were cultured in Dulbecco's Modified Eagle Medium with high glucose (4.5 g/L D-glucose; Carl Roth GmbH+Co.KG, Karlsruhe, Germany), supplemented with 10 % fetal calf serum (Sigma Aldrich, Taufkirchen, Germany). Cells were maintained at 37 °C in a humidified incubator with 5 % CO_2.

For CLEM experiments, cells were seeded into MatTek dishes (MatTek, Ashland, MA, USA) with a gridded and removable coverslip, to enable imaging under the confocal microscope as well as FIBSEM. For the incubation times of 2 and 6 h, as well as the control samples, 150.000 cells were seeded into each dish. For the 24 h IOH-NP incubation, 90.000 cells were seeded in each dish. Cells are maintained in the incubator over night to ensure proper attachment. Control cells are referred to as H8N8 cells without the addition of IOH-NPs.

IOH-NPs

$[ZrO]^{2+}[(CMP)_{0.99}(DUT647)_{0.01}]^{2-}$ IOH-NPs were prepared by dissolving 36.7 mg (0.1 mmol) of cytidine monophosphate sodium salt (Na_2(CMP), ≥ 97 %, Sigma Aldrich, Taufkirchen, Germany) in 50 mL of demineralized water. For fluorescence labelling, 25 nmol of DUT647 were added to the $[CMP]^{2-}$ solution. Thereafter, 0.5 mL of an aqueous

solution containing 29.3 mg (0.09 mmol) of $ZrOCl_2{\cdot}8H_2O$ (99.9 %, Sigma Aldrich, Taufkirchen, Germany) were injected, which resulted in an instantaneous nucleation of IOH-NPs. After 2 min of intense stirring, the as-prepared IOH-NPs were separated via centrifugation (25.000 rpm, 15 min) and twice purified by redispersion/centrifugation in/from H_2O. For further use, the IOH-NPs were dispersed in demineralized water or dried to powder samples. Further details of synthesis and analytical characterization were previously published in.[3]

For the following CLEM experiments, IOH-NPs with 50–60 nm in size were used in a concentration of 10 μg/mL. For this purpose, an aliquot of the IOH-NP stock suspension in demineralized water was thoroughly resuspended and subsequently diluted in complete cell culture medium. A total of 2 mL of this working solution were added to each dish and incubated for the desired time periods of 2, 6 and 24 h at 37 °C and 5 % CO_2. After incubation, the IOH-NP-containing medium was removed and exchanged by the desired staining solution for further fluorescent staining. To prevent IOH-NPs from clustering, they were stored at 4 °C on a shaker, protected from light.

Confocal imaging and stainings

30 min before the end of the IOH-NP incubation time, cells were stained with LysoTracker Blue DND-22 (500 nM; Thermo Fisher Scientific, Waltham, MA, USA) and BODIPY 493/503 (5 μM; Thermo Fisher Scientific, Waltham, MA, USA). Afterwards, the samples were taken to the confocal microscope (Zeiss LSM 700 (Zeiss, Oberkochen, Germany)). Images were captured using the wavelengths of 405 nm (LysoTracker), 488 nm (BODIPY) and 639 nm (DUT647 - IOH-NPs). To choose cells of interest, a 10× objective was first used to identify the grid pattern and find the same cell again in FIBSEM. Afterwards, chosen cells were imaged with a 63× oil immersion objective at high resolution. 3D image stacks were acquired along the *Z*-axis to enable volumetric reconstruction of cellular structures. Subsequent processing, such as noise reduction and contrast enhancement, was performed using Fiji software.[25]

Chemical fixation

Immediately after confocal imaging, the cells were fixed with 2 % paraformaldehyde (Electron Microscopy Sciences, Hatfield, PA, USA) and 2.5 % glutaraldehyde (Electron Microscopy Sciences, Hatfield, PA, USA) in 0.1 M sodium cacodylate buffer (Electron Microscopy Sciences, Hatfield, PA, USA) for 2 h at 4 °C. Afterwards, the samples were carefully washed multiple times with 0.1 M cacodylate buffer. Next, the samples were stained with reduced osmium, which contains 1 % osmium (OsO4, Electron Microscopy Sciences, Hatfield, PA, USA), 1.5 % K_4FeCN_6 (Carl Roth, Carl Roth GmbH+Co.KG, Karlsruhe, Germany) in 0.1 M cacodylate buffer for 2 h at 4 °C. The samples were gently washed with cacodylate buffer again and then set into 0.3 % thiocarbohydrazide (Electron Microscopy Sciences, Hatfield, PA, USA) for 30 min at room temperature. Samples were washed again and stained with 1 % OsO4 for another 2 h at 4 °C with gentle washing with water afterwards. Next, the cells were stained with 1 % uranyl acetate (Electron Microscopy Sciences, Hatfield, PA, USA) overnight at 4 °C. Samples were washed with water again and then dehydrated with graded ethanol series (25, 50, 75, 90, 100 %) for 10 min each. Afterwards samples were infiltrated stepwise with mixtures of durcupan resin (Merck KGaA, Darmstadt, Germany and ethanol (1: 2, 1: 1, 2: 1; 20 min each) followed by a step pf pure durcupan infiltration, after which they were polymerized at 60 °C for 48 h. After hardening, the cell containing part was removed from the dish and glued with a thin layer of resin onto a SEM stub. The edges of the sample were painted with conductive silver ACHESON 1415 (PLANO GmbH, Wetzlar, Germany).

FIBSEM imaging

Embedded samples were shuttled into the Zeiss Crossbeam 550 and ROIs of cells, identified previously by light microscopy, were targeted using Zen blue connect (Zeiss, Oberkochen, Germany), overlaying images from the light microscope and the SEM. A trench was milled and the cross-section of the cell was polished after applying a 500 nm thick platinum coat using the gas injection system on the top of the sample surface. Data acquisition was done at 1.5 kV, 1000 pA with a pixel size of 5 nm (x/y) with 15 nm distance between individual slices using the EsB detector with a grid voltage of 450 V. Images were acquired with a dwell time of 2 μs and a line averaging of 5. Iterating between milling and imaging a FIB beam of 30 kV, 700 pA was used.

The FIBSEM datasets were aligned using a re-implementation of the AMST approach that includes a coarse pre-alignment step (https://github.com/jhennies/AMST2/). For the coarse pre-alignment step, the Simple Elastix package[26] was used to determine offsets between adjacent slices (short distance) and every eighth slice (long distance). Application of the combination of both offsets (short distance and interpolated long distance offsets) resulted in a very stable morphologically sensible coarse alignment. For fine-tuning the alignment, in order to correct for non-linear deformations of image slices, we used the AMST workflow[27] adjusted for a b-spline transformation where the z-median filtered template was computed with a radius of 7 slices. To further enhance the data, Contrast Limited Adaptive Histogram Equalization (CLAHE) with subsequent Gaussian filtering was applied.

Correlation of confocal FM and FIBSEM datasets

In general, the re-identification of the cell of interest between confocal microscopy and FIBSEM was successfully applied by first imaging the H8N8 cells live under the confocal microscope using a 10× objective combined with the transmission light channel using gridded MatTek dishes. This enabled the identification of the imprinted grid (**Fig. 1A** and **B**), and a ROI was chosen. A high magnification image of the chosen region is shown in Fig. 1C. After chemical fixation, the same region can be found and imaged using FIBSEM (Fig. 1D-F).

The confocal FM and FIBSEM stacks were correlated based on lipid droplet, stained with BODIPY for their detection in the FM channel (compare Results).

Image processing to quantify the cellular interaction with IOH-NPs

Cells were seeded into ibidi μ-dishes (Ibidi GmbH, Graefelfing, Germany) with approximately 50.000 H8N8 cells per dish. After 24 h, IOH-NPs were added to the cells with a concentration of 10 μg/mL. Cells were stained with LysoTracker Blue DND-22 (500 nM; ThermoFisher Scientific, Waltham, MA, USA) and MitoTracker Green FM (50 nM, ThermoFisher Scientific, Waltham, MA, USA) for 30 min. MitoTracker was later used to facilitate the segmentation of single cells and the quantification of the IOH-NP uptake (compare Fig. 2). At distinct timepoints after IOH-NP incubation (1, 2, 4, 6, 14, 24, 48 h), live H8N8 cells were imaged using the confocal microscope Zeiss LSM 700. The microscopy images were processed and analyzed using the software Fiji[25] and CellProfiler.[28] Using custom-designed pipelines with several modules, as can be seen in Fig. 2, the percentage of cells with IOH-NP uptake, the uptake quantity, and interaction of endolysosomal vesicles with IOH-NPs were quantified for all time points.

For the analysis of the images, first, the .czi *Z*-stack files created in ZEN were separated into the four individual channels (transmitted light, mitochondria, endolysosomal vesicles and IOH-NPs) using a Fiji macro, converted into .tiff files and Z-stacks were generated as maximum intensity projections (MIPs), whereby, for each pixel in the XY plane, the highest intensity value along the Z-axis is selected to create a two-dimensional image that depicts the maximum visible structures from all levels of the stack.

For segmentation, the images of the mitochondrial and endolysosomal channels were used, which were processed the same way and then merged. During processing, a white tophat filter was first applied to

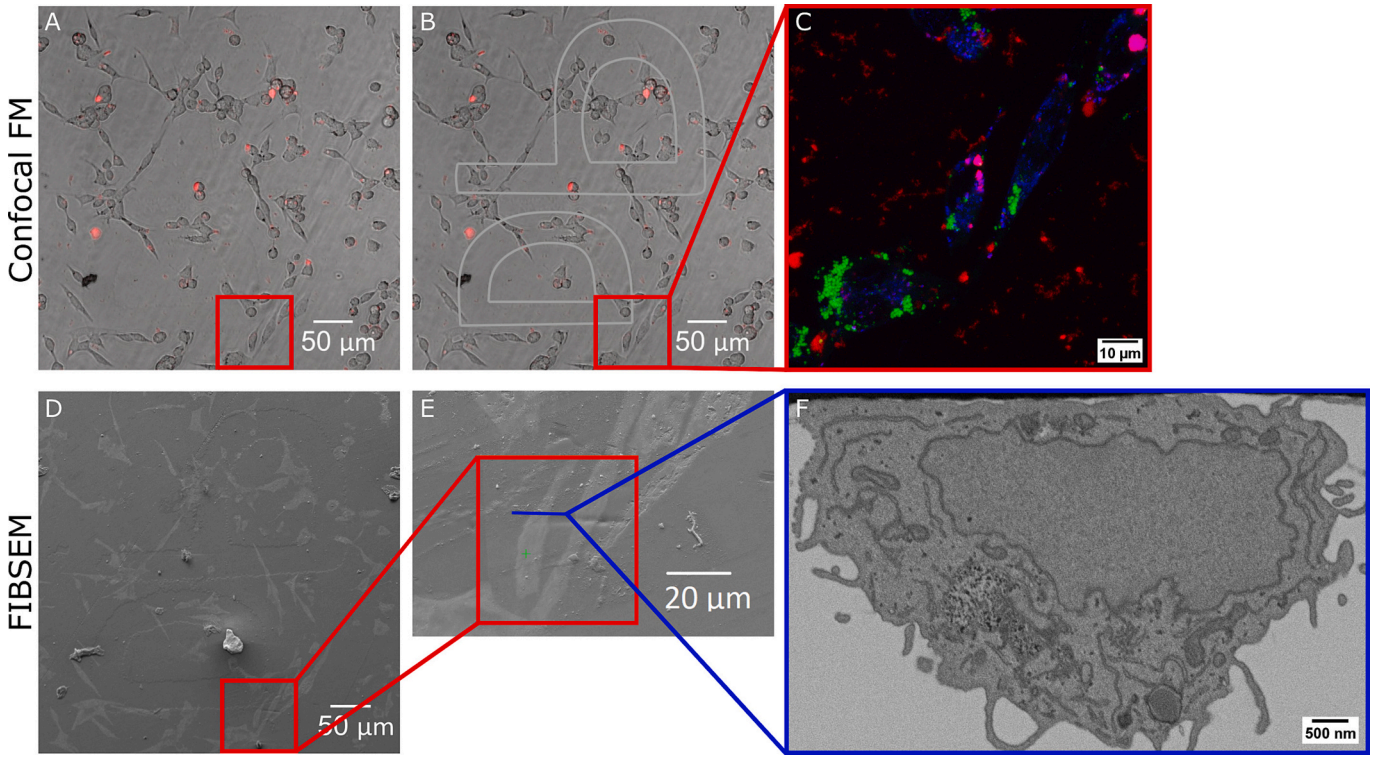

Fig. 1. General CLEM workflow set up based on gridded MatTek dishes to re-identify cells of interest between confocal FM and FIBSEM. Low magnification FM images (A) and (B) show the grid region "PD", where in (B) the outline of the letters was drawn onto the image for better visualization. Red boxes mark the ROI that was imaged by the 63× objective. (C) shows the maximum intensity projection (MIP) of the ROI of the cells stained with LysoTracker (blue), BODIPY (green) and IOH-NPs (red), incubated for 2 h and observed with the 63× objective. (d) shows the same region as (A) and (B) using FIBSEM with low magnification, the red box marks the same ROI as above. (E) shows the same field of view as in (C) in FIBSEM, and (F) a single slice imaged by FIBSEM in the XZ-plane. The blue box highlights the image section through the cell using FIBSEM.

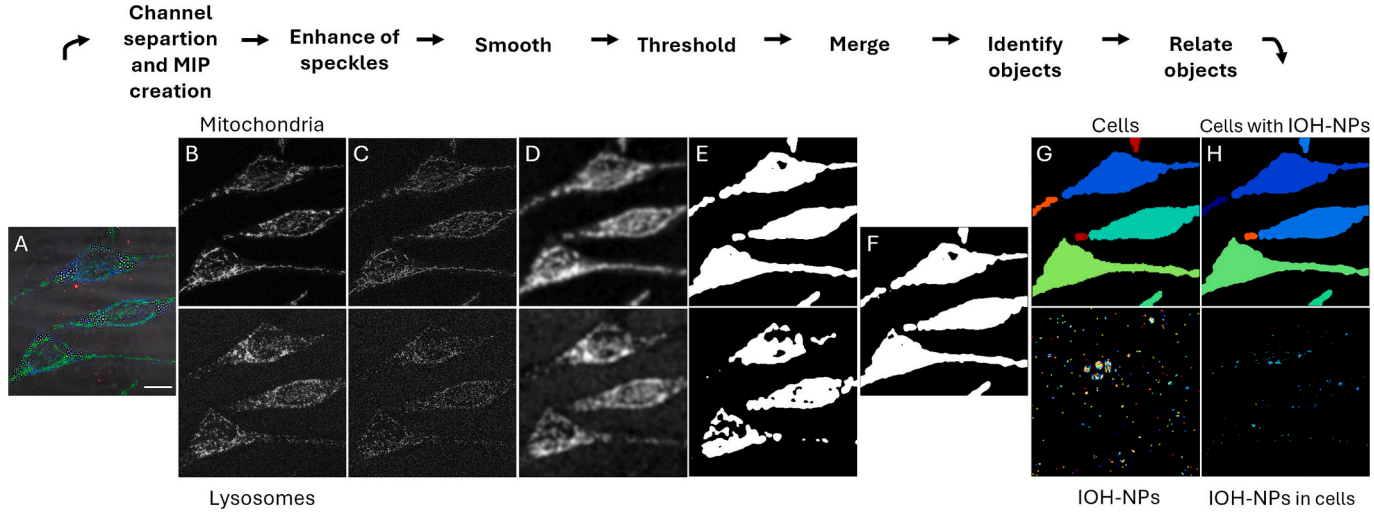

Fig. 2. Image processing workflow for the quantification of IOH-NP uptake into H8N8 cells. Scale bar is the same for all images, 10 µm. (A) Composite slice of H8N8 cells, incubated with IOH-NPs (red) and stained with LysoTracker (blue) and MitoTracker (green). (B) First, the FM channels were separated (mitochondria and endolysosomal vesicles) and maximum intensity projections of each were created. (C) Next a white tophat filter was applied to enhance speckles, followed by smoothing via a gaussian filter (D). Created cell segments were binarized via thresholding (E), and both channels were merged again (F). Otsu thresholding enabled identification of single cells (top) and adaptive thresholding with robust background to identify IOH-NPs (bottom) (G). Relating the area (pixel sizes) of the IOH-NPs and that of the segmented cells allowed for the quantification of IOH-NP subcellular concentrations (H) – after visually checking that segmented IOH-NPs and cells overlap.

enhance the speckles, followed by a Gaussian filter as a smoothing method. A global thresholding strategy using the minimum cross-entropy method was then applied. After the processed images of the channels were merged, the cells were identified as primary objects using global Otsu thresholding, with the lower and upper bounds of the threshold of 0.5–1.0. The IOH-NPs were identified using adaptive thresholding with a robust background. This pipeline is shown in Fig. 2.

A total of 677 cells were analyzed for these quantitative assessments

(1 h – 75 cells, 2 h – 132 cells, 4 h – 60 cells, 6 h – 93 cells, 14 h – 91 cells, 24 h – 114 cells, 48 h – 112 cells).

The identified objects were then related to each other to assess the following parameters:

1. To determine the rate of IOH-NP uptake by the H8N8 cells, we set up the image processing workflow as described in Fig. 2. The analysis was completed by visual screening of the images in the ZEN program to validate cell count and IOH-NP uptake (# of cells with IOH-NPs in %).
2. IOH-NP uptake intensity (% IOH-NPs in cells) was determined accordingly. Additionally, a module measuring the image area occupied by cells and the area occupied by cell-related IOH-NPs was used to quantify the percentage of correlation over time.
3. To assess the endolysosomal association of the engulfed IOH-NPs (% IOH-NPs in endolysosomal vesicles in relation to total IOH-NPs in cells), lysosomes were identified from the MIP images of the endo-lysosomal channel using a global Otsu thresholding method. Based on this, the occupied image area was measured and related to that of the internalized IOH-NPs.

To determine the endolysosomal volume (% per cell area), the individual images of the *Z*-stack of the mitochondrial and endolysosomal channels were extracted using Fiji. Each image was then processed and segmented as described in (2) to determine the total cell volume. For the endolysosomal volume, the images were processed analogously to (3).

Results

Using lipid droplet-based CLEM, IOH-NPs were unambiguously identified in 3D FIBSEM datasets

Confocal FM was used to monitor the distribution and interaction of IOH-NPs (red), endolysosomal vesicles (blue), and lipid droplets (green) over time. Using the 3D-CLEM approach based on the correlation via lipid droplets, confocal FM and FIBSEM datasets were aligned such that IOH-NPs and lysosomes were unambiguously identified within the FIBSEM images in 3D without the need for external fiducial markers (Fig. 3) for correlation, such as fluorescent and electron-dense microspheres or quantum dots. Here, the lipid droplets served as correlation landmarks across modalities. The 3D-CLEM data were acquired at timepoints of 2, 6, and 24 h, as well as for control cells without the addition of IOH-NPs for reference.

IOH-NPs are internalized within one hour, with a significant increase of IOH-NP concentrations in both cells and endolysosomal vesicles over time

Following IOH-NP exposure, the IOH-NPs rapidly formed clusters and were taken up via endocytosis within 1 h, with intracellular concentrations increasing over time. These findings are highlighted by

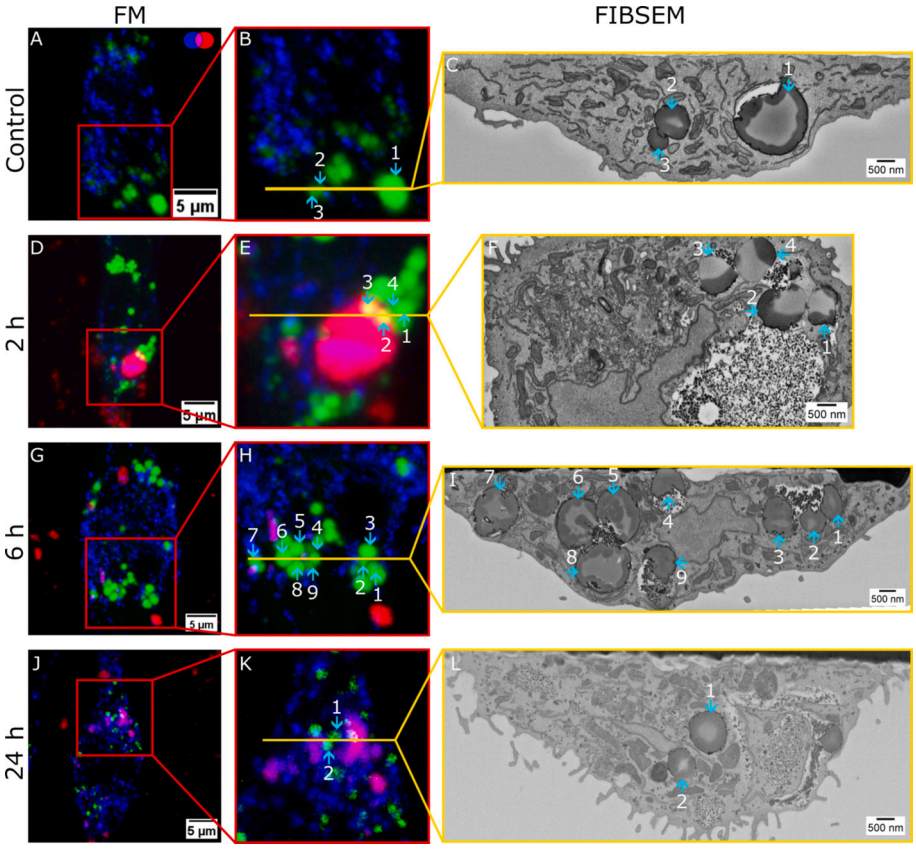

Fig. 3. 3D-CLEM workflow based on lipid droplets for the unambiguous identification of IOH-NPs. Cells were stained with LysoTracker (blue) and BODIPY (green). Control cell (A-G): (A) MIP with red box showing the ROI. (B) Magnified ROI, the yellow line indicates the localization of the FIBSEM cross section (XY plane), shown in (C). Cyan arrows with numbers show lipid droplets, which can be identified in (B, C). For better visualization (D) shows the area of the FIBSEM section also as a MIP of the FM channel and the marked lipid droplets. (F) shows another FIBSEM section with a lysosome marked in blue. The corresponding area in FM is again marked in (E) and (G). In contrast to cells exposed to IOH-NPs, the lysosome of the control appears homogeneous and does not show any internalized NP-resembling structures. (H) shows a MIP of a cell incubated with IOH-NPs for 24 h (IOH-NPs shown in red, overlap of IOH-NPs and endolysosomal vesicles in magenta. The red box shows the ROI of (J). The yellow line in (I) corresponds to the magnified FM region in (K) and the FIBSEM section (XY plane) shown in (J). Correlated lipid droplets are marked both in the FM and FIBSEM channels by cyan arrows and numbers, and correlated IOH-NPs within endolysosomal vesicles are marked both in the FM and FIBSEM channels by red arrows and letters.

representative time-lapse confocal MIP images that show H8N8 cells stained with LysoTracker Blue, MitoTracker Green and IOH-NPs at different incubation times between 1 h and 48 h (Fig. 4**,** Fig. 5). The zoomed-in areas in Fig. 4 indicate an increase in IOH-NP uptake over time, as also confirmed and complemented using 3D-CLEM (Fig. 6). We also showed that every H8N8 cell had taken up IOH-NPs after 4 h.

The quantification of the IOH-NP uptake rate by H8N8 cells (number of cells with IOH-NPs in %) showed that, after 1 h, an average of 80 % of the cells had internalized an amount of IOH-NPs that was detectable using confocal FM. After 4 h, every single cell examined had internalized several IOH-NPs. This persisted throughout the 48-h observation period (Fig. 5A**).**

Additionally, the intracellular concentration of IOH-NPs was quantified as described in the methods section (compare 2.7 and Fig. 2) by calculating the ratio of the area occupied by IOH-NPs and that of the segmented cells. The quantification of the amount of IOH-NPs that was taken up by the cells (IOH-NP uptake intensity, i.e. % IOH-NPs in cells) revealed that longer incubation times led to a significantly higher IOH-NP uptake. Over the course of 48 h, IOH-NPs progressively accumulated within the cells and specifically in endolysosomal compartments (Figs. 5B, C**)**. This increase in uptake was accompanied by an increase in variance at longer time points. While a significant increase in IOH-NP uptake was recorded between 6 h to 24 h (from (2.6 ± 1.4) % to (6.1 ± 1.9) %), after 24 h, IOH-NPs seemed to have reached a steady state between uptake and dissolution since there was no significant increase in IOH-NP concentration neither in the cells nor in the endolysosomes compared to 48 h**.** This might be due to a continuous uptake that is accompanied the simultaneous dissolution of IOH-NPs by endolysosomal vesicles (compare Fig. 6).

With longer IOH-NP incubation times, we also measured a significantly increased uptake into endolysosomal vesicles of the IOH-NPs by quantifying the endolysosomal association of IOH-NPs (% IOH-NPs in endolysosomal vesicles in relation to total IOH-NPs in cells) (Fig. 5C**)**. Notably, the overall endolysosomal volume expanded between 2 and 6 h post-incubation, but subsequently returned to baseline and remained stable throughout the 48 h observation period (Figs. 5D**)**, indicating an endolysosomal reaction of the cancer cells to a first exposure to IOH-NPs.

The observations were further confirmed using 3D-CLEM. The FIBSEM images in Fig. 6 depict a representative uptake of the IOH-NPs within endolysosomal vesicles after 6 h and 24 h incubation times. This confirms that the IOH-NPs enter cells via the endocytic pathways and are trafficked into the endolysosomal system, shown by red arrowheads in Fig. 6, a common route for IOH-NP internalization.[29,30] The FIBSEM datasets also revealed that, over time, IOH-NPs were increasingly found in endolysosomal compartments. Inside the lysosomes, we also observed changes in the morphology and density of the IOH-NPs, suggesting that the dissolution of some IOH-NPs already started within 2 h. Fig. 7 shows a large cluster of IOH-NPs within the cell, detected by the red fluorescent signal in the FM channel. Part of this cluster is located within an endolysosomal vesicle, shown by the magenta color of the FM slice due to the overlap with endolysosomal vesicles stained in blue. The correlated FIBSEM image shows the cluster within an endolysosomal vesicle. The lysosome-associated IOH-NPs are smaller in diameter, have less intensity and appear more disperse, which suggests that IOH-NP are dissolved in part within the endolysosomal vesicles. Particularly, this contrasts with the homogeneous appearance of IOH-NPs that were internalized by the cells, but were not taken up by lysosomes as shown in Fig. 8**:** This is demonstrated both in the FM channel, where no lysosomal colocalization (LysoTracker in blue) can be seen and in the FIBSEM image, where the IOH-NPs are not delineated by membranes as would be the case for endolysosomal vesicles (compare for example IOH-NP clusters in lysosomes in Figs. 3J, 6B and D). Interestingly, IOH-NPs were hence not found exclusively in lysosomes, but also in the cytoplasma.

Qualitative analysis suggests that IOH-NP uptake itself can lead to ultrastructural changes in H8N8 cancer cells

In addition to endolysosomal accumulation and dissolving of the IOH-NPs, 3D-CLEM analyses also indicated morphological changes in tumor cells that were only observed in cells that had taken up IOH-NPs and not in control cells. Fig. 9 shows FIBSEM reslices in XY plane, where, in **Figs. 9C** and **D,** orange arrowheads mark swollen mitochondria within a H8N8 cell after 6 h of IOH-NP treatment, compared to normal-sized mitochondria in **Figs. 9A** and **B** in control cells. After 24 h of IOH-NP incubation, we additionally observed disruptions within the cancer cells in FIBSEM images, as shown in **Fig. 9E** and **F**, where the zoomed-in area in **9D** shows that these inclusions are in part enclosed by a membrane, and in part remain free of any contrast-stained molecules or elements. Whether these structural changes are alterations in response to IOH-NP treatment or whether they occur due to artefacts in the sample preparation needs further analysis.

Discussion

In this study, we successfully established a 3D-CLEM workflow that enabled the unambiguous visualization of IOH-NPs in breast cancer cells within their ultrastructural context by combining confocal FM with FIBSEM without the need to add external correlative markers, such as fluorescent and electron-dense microspheres or quantum dots. Correlation was established through endogenous lipid-droplet markers since they are clearly identified in both modalities, in FM due to fluorescent staining and in FIBSEM due to their electron dense properties. The IOH-NPs were then clearly identified in both imaging modalities based on their fluorescence and electron absorbance. Hitherto, correlation is achieved manually by analyzing and comparing the position of lipid droplets in both modalities to relocate specific positions. Scher et al. (2021)[14] previously suggested the use of lipid droplets as in situ fiducial markers for CLEM. While their approach targeted the registration between cryogenic modalities (FM and FIBSEM), we here demonstrated the feasibility of lipid droplet-based CLEM at room temperature and its application to a biomedical research question for the unambiguous identification of NPs as a novel drug delivery system. This aligns with their paper, which concludes by noting that the lipid-droplet–based CLEM 'workflow can be used to address different questions in cell biology, where resolving the ultrastructural organization of the cell at its native state is important.' Extending this concept, we demonstrate the utility of lipid-droplet fiducials for dynamic biomedical investigations that emphasize time-resolved cellular tracking rather than cryogenic preservation.

We aim at automating this process by automated segmentation and subsequent registration of the lipid droplets in both imaging modalities.[31,32] While the workflow provided highly resolved, correlated 3D data that offered valuable insights into IOH-NP-cell interactions at the ultrastructural level and demonstrated the strength of advanced CLEM approaches in nanomedicine research, automation will be crucial since the 3D-CLEM workflow is still significantly limited by throughput: FIBSEM data acquisition itself is highly time-consuming, often requiring at least one day of continuous imaging per single cell to obtain a complete volumetric dataset at nanometer resolution. Moreover, the chemical fixation and sample preparation for FIBSEM itself is a complex, multi-day process involving several staining and dehydration steps. The success of this protocol strongly depends on the careful preparation of all solutions; inadequate preparation can significantly reduce contrast in EM images and thus additionally limit the throughput and interpretability of the data.

Using the established 3D-CLEM workflow, we were able to directly visualize the uptake of IOH-NPs into H8N8 breast cancer cells. 3D-CLEM showed that IOH-NPs increasingly accumulate in cancer cells and endolysosomal vesicles over time. This supports the hypothesis that IOH-NPs primarily enter cells via endocytic pathways. Beyond uptake,

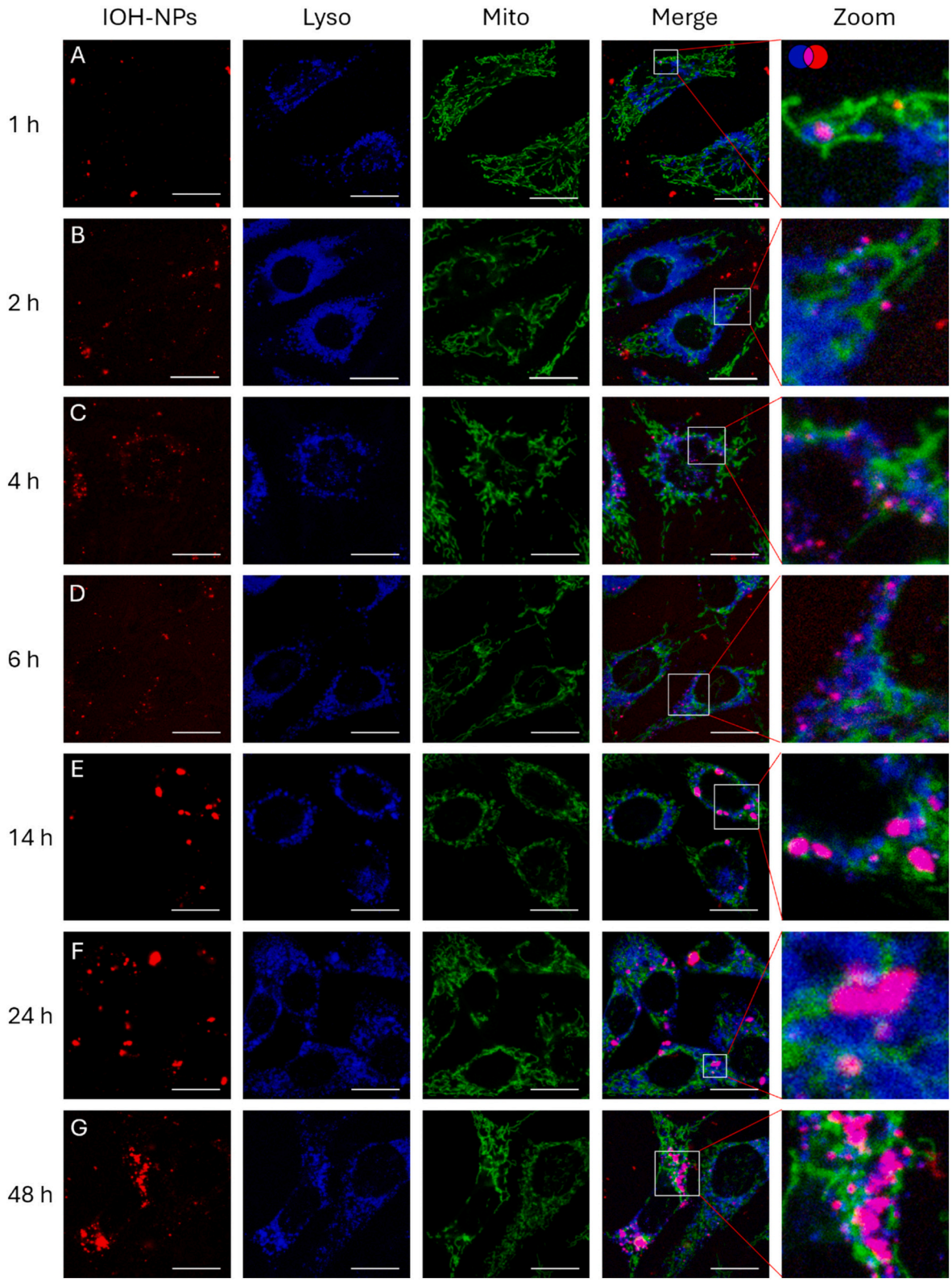

Fig. 4. Confocal MIP images of H8N8 cells stained with LysoTracker (blue), MitoTracker (green) and IOH-NPs (red), showing increased uptake of IOH-NPs into cancer cells and endolysosomal vesicles over time. Scalebar: 20 μm. The confocal MIP images were separated into their individual channels, showing IOH-NPs in red, endolysosomal vesicles in blue and mitochondria in green. The merged column represents all channels within one image. The white boxed indicate the ROIs that are magnified in the 'zoom' column. Row (A) shows a H8N8 cell after 1 h IOH-NP incubation, revealing a small overlap between IOH-NPs and endolysosomal vesicles within a small area in the zoomed-in image (white square). (B, C) show the intracellular uptake of IOH-NPs after 2 and 4 h, representing the steady increased uptake into lysosomes over time. After 6 h IOH-NP incubation, the co-localization of endolysosomal vesicles and IOH-NPs is already significantly increased (D). After longer IOH-NP incubation times, the uptake of IOH-NPs into lysosomes keeps increasing up to a constant value after 24 h, as highlighted for a representative time-lapse series after 14 (E), 24 (F), and 48 h (G).

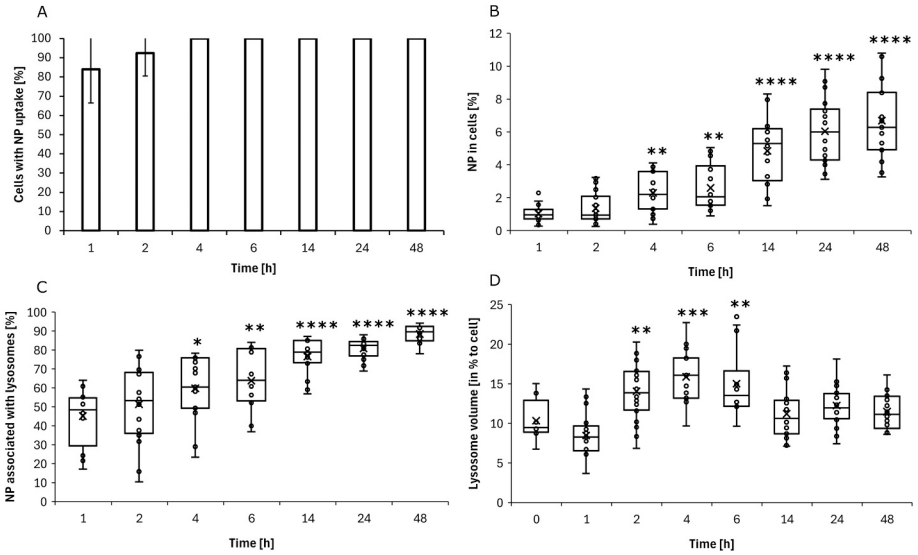

Fig. 5. Quantitative analysis of IOH-NP-cell-interaction. (A) Cells with IOH-NP uptake [%], showing that after 4 h incubation, IOH-NPs can be found in every cell. (B) Fraction of IOH-NPs in cells [%], revealing that cellular uptake of IOH-NPs increases significantly over time until reaching a steady state after 24 h. (C) IOH-NPs co-localizing with endolysosomal vesicles [%], showing that also the interaction between IOH-NPs and endolysosomal vesicles increased significantly over time, until reaching a plateau after 24 h. (D) Endolysosomal volume over time [% to cell], timepoint 0 indicating cells without IOH-NP treatment, showing an increase of endolysosomal volume after 2 h of IOH-NP incubation time. Following a decrease after 6 h, endolysosomal volume remained steady during the observation period. *: $p < 0.05$, **: $p < 0.01$, ***: $p < 0.001$, ****: $p < 0.0001$. The t-test assessed significance in relation to the 1-h IOH-NP treatments and for the quantification of the endolysosomal volume to the control cells (marked as 0 h).

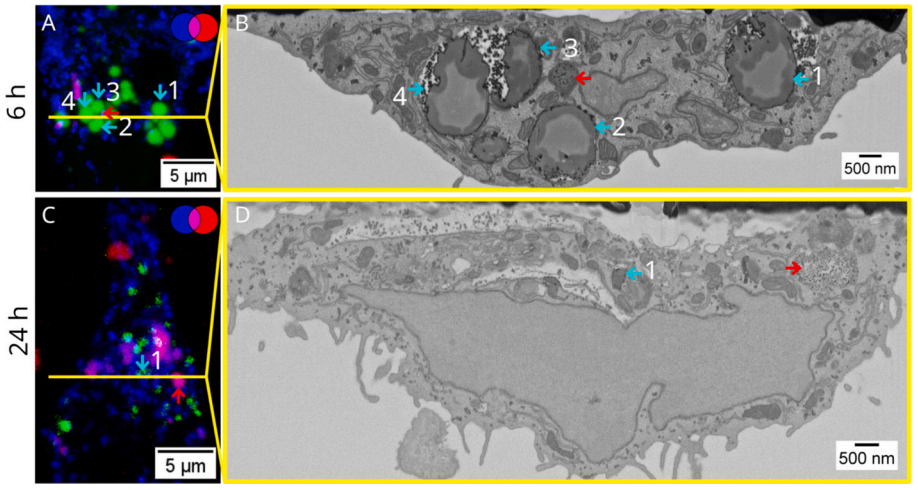

Fig. 6. 3D-CLEM reveals increased IOH-NP uptake into endolysosomal vesicles over time. (A, C) show FM MIP images of 6 and 24 h IOH-NP incubation. Yellow lines indicate the positions shown in FIBSEM images in (B, D). Red arrows highlight correlated IOH-NPs within endolysosomal vesicles in FM and FIBSEM, cyan arrows and corresponding numbers indicate the same lipid droplets in FM and FIBSEM.

we also observed morphological changes of the IOH-NPs themselves inside endolysosomal vesicles by FIBSEM, which suggests a gradual dissolution of the IOH-NPs. Such alterations likely reflect the initial stages of IOH-NP degradation in the acidic and enzyme-rich environment of endolysosomal vesicles, which is an important step for the potential release of the drug cargo, for example chemotherapeutic drugs to reach the nucleus.

Interestingly, after 6 h of incubation, we detected pronounced ultrastructural changes in cancer cells exposed to IOH-NPs, including increased mitochondrial sizes and disrupted organelles. Although this observation suggests that IOH-NP uptake might influence mitochondrial morphology and potentially the cellular metabolism even without drug load, the data is currently too limited to draw general conclusions – specifically, artefacts due to sample preparation cannot be ruled out. Given the high effort required for FIBSEM, we plan to address this question in follow-up experiments using FM to systematically quantify mitochondrial volumes over different incubation times. In addition, we will perform MTT assays to assess possible effects on mitochondrial activity and cell viability in response to IOH-NP exposure.

Another aspect relates to the intracellular fate of the IOH-NPs over extended periods. Between 24 h and 48 h of incubation, the overall IOH-NP concentration inside the cells did not change significantly, suggesting limited further uptake or release or dissolution mechanisms. To better understand whether IOH-NPs are retained or actively exocytosed or dissolved, a dedicated degradation and clearance study will need to be carried out, including the removal of extracellular IOH-NPs after an initial incubation period and monitoring intracellular IOH-NP content over time.

Despite the observed IOH-NP clustering, H8N8 cells were able to take up high concentrations of IOH-NPs. Reducing IOH-NP aggregation

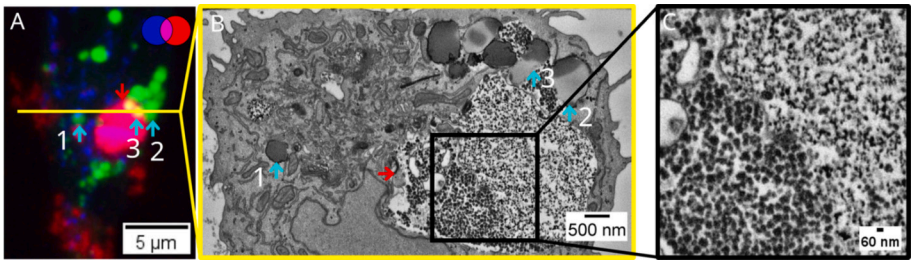

Fig. 7. Heterogeneity of IOH-NP appearance within lysosomes. (A) Representative FM MIP image that shows lipid droplets in green, lysosomes in blue, and intracellular IOH-NPs (incubated for 2 h) in red. The overlap between IOH-NPs (red) and lysosomes (blue) is depicted in magenta; the overlap between IOH-NPs (red) and lipid droplets (green) in indicated in yellow. Cyan arrows highlight lipid droplets that were correlated with the FIBSEM section shown in (B); red arrows highlight a correlated IOH-NP cluster within a lysosome in both FM and FIBSEM channels. The yellow line indicates the cross section through the cell that is visualized using FIBSEM in (B). The black box indicates a ROI within the IOH-NP cluster within the lysosome and is depicted as a magnified, zoomed-in image in (C). Here, the heterogenous appearance of the IOH-NPs (different densities and sizes below 60 nm of the IOH-NPs) suggests a dissolution of the IOH-NPs by the acidic environment of the lysosome.

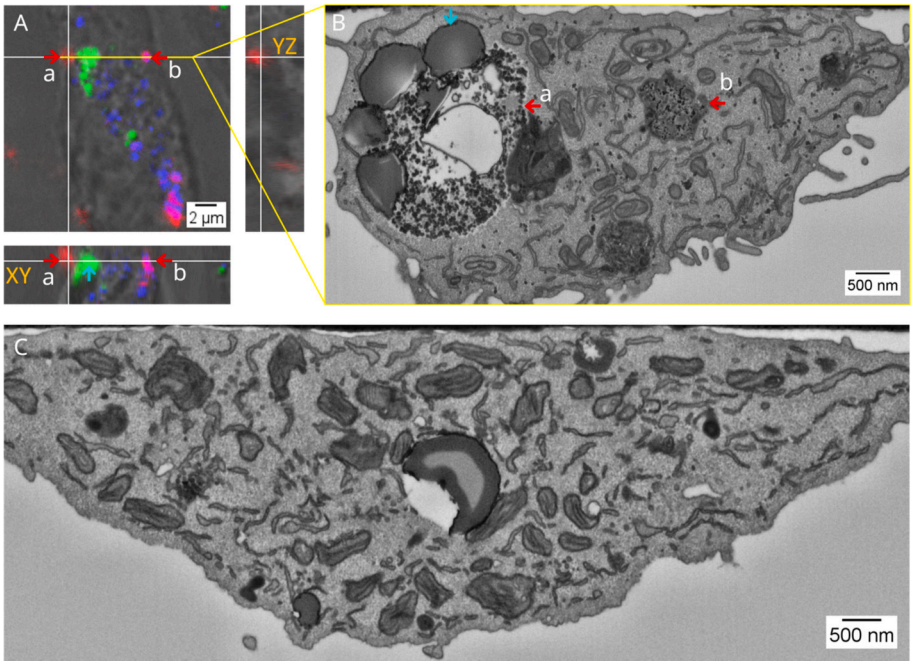

Fig. 8. IOH-NPs were also found in other compartments than endolysosomal vesicles. (A) FM orthoslice showing IOH-NP cluster without endolysosomal association (red arrow in YZ plane) after 2 h of IOH-NP incubation. (B) FIBSEM cross section of the ROI (yellow line in (A)), where an IOH-NP cluster is not membrane delineated and is found within the cytoplasm. It is marked with a red arrow as a. The same cell also highlights an IOH-NP cluster (marked as b) that is delineated by membranes as seen in the FIBSEM channel and shows magenta color, i.e. overlap with lysosomes, in the FM channel. Interestingly, single IOH-NPs were also detected (B) throughout the cytoplasm – but cannot be unambiguously identified due to the lack of visibility of single IOH-NPs within FM MIP images. Cyan arrows mark correlated lipid droplet in the FM orthoslice YZ and the FIBSEM image. For comparison (C) shows a FIBSEM slice of a H8N8 cell without IOH-NP treatment (control), where no black dots representing IOH-NPs can be identified.

nevertheless remains an important factor in improving uptake efficiency during tumor treatment. Potential IOH-NP modifications to avoid clustering and promote better dispersion in physiological environments include surface functionalization with polyethylene glycol (PEG), lipid coating to enhance colloidal stability, or introducing steric or electrostatic repulsion via charged or bulky surface groups.

Together, these findings highlight the value of 3D-CLEM for unraveling the complex dynamics of IOH-NP uptake, intracellular processing, and potential clearance pathways.

CRediT authorship contribution statement

Louisa Herbsleb: Writing – review & editing, Writing – original draft, Visualization, Validation, Methodology, Investigation, Formal analysis, Data curation. **David Wild:** Visualization, Validation, Methodology, Investigation, Formal analysis, Data curation. **Henriette Gröger:** Resources. **Tim Schubert:** Resources, Data curation. **Anna Maria Steyer:** Visualization, Resources, Methodology, Data curation. **Julian Hennies:** Visualization, Software, Resources. **Frauke Alves:** Writing – review & editing, Conceptualization. **Claus Feldmann:** Writing – review & editing, Resources, Conceptualization. **Andreas Walter:** Writing – review & editing, Writing – original draft, Validation, Supervision, Project administration, Methodology, Funding acquisition, Conceptualization.

Funding sources

Carl Zeiss Stiftung within the call CZS Transfer 2024: Oberflächen.

We acknowledge funding from the Carl Zeiss Stiftung within the call CZS Transfer 2024: Oberflächen.

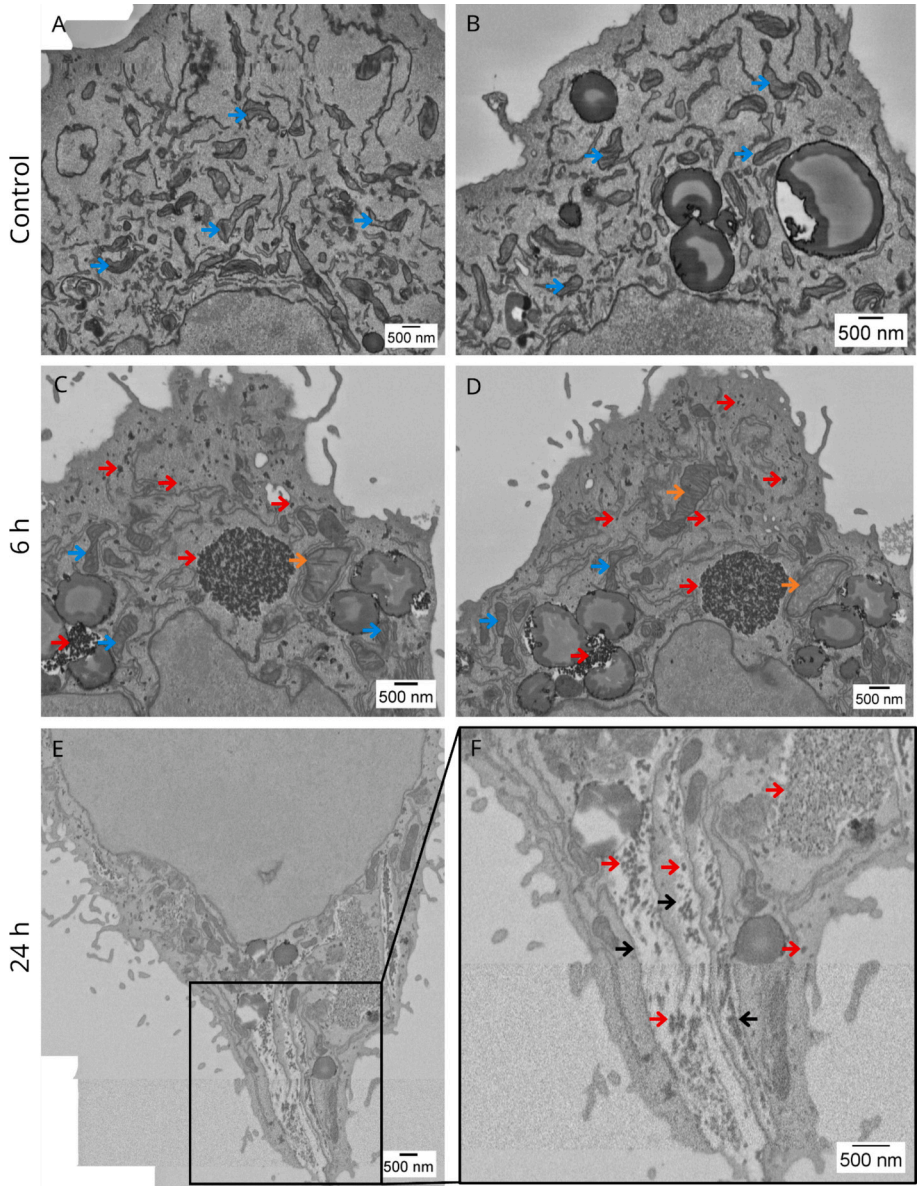

Fig. 9. Ultrastructural changes in cancer cells after IOH-NP exposure. FIBSEM reslices (XY plane) of H8N8 cells without IOH-NP treatment as control (A, B) and with IOH-NP incubation of 6 h (C, D) show a significant increase in mitochondrial sizes, as shown by orange arrowheads after IOH-NP treatment. Blue arrowheads point to normal-sized mitochondria. (E) shows a FIBSEM slice (XY plane) with visible disruptions within the cell after incubation with IOH-NP incubation of 24 h. (F) shows a zoomed-in region of (E) (black box), showing that the disruptions (black arrowheads) were partially enclosed by a membrane, while other parts were not surrounded by any contrast-stained structures, which was not observed in control cells. Based on the previous correlation, IOH-NPs are marked in red.

We acknowledge funding from the Chan Zuckerberg Initiative within the call Advancing Imaging Through Collaborative Projects (COMULISglobe).

Acknowledgements

We acknowledge the access and services provided by the Imaging Centre at the European Molecular Biology Laboratory (EMBL IC), generously supported by the Boehringer Ingelheim Foundation.

We acknowledge the Carl Zeiss Stiftung with funding within the call CZS Transfer 2024: Oberflächen.

We acknowledge COMULISglobe for supporting the research conducted for this publication.[33]

References

1. Heck JG, Napp J, Simonato S, Möllmer J, Lange M, Reichardt HM, et al. Multifunctional phosphate-based inorganic-organic hybrid nanoparticles. *J Am Chem Soc*. 2015;137(23):7329–7336. https://doi.org/10.1021/jacs.5b01172.
2. Ischyropoulou M, Sabljo K, Schneider L, Niemeyer CM, Napp J, Feldmann C, et al. High-load gemcitabine inorganic-organic hybrid nanoparticles as an image-guided tumor-selective drug-delivery system to treat pancreatic cancer. *Adv Mater*. 2023;35 (46), e2305151. https://doi.org/10.1002/adma.202305151.
3. Khorenko M, Pfeifer J, Napp J, Meschkov A, Alves F, Schepers U, et al. Theranostic inorganic-organic hybrid nanoparticles with a cocktail of chemotherapeutic and cytostatic drugs. *J Mater Chem B*. 2023;11(16):3635–3649. https://doi.org/10.1039/d3tb00226h.
4. Sabljo K, Ischyropoulou M, Napp J, Alves F, Feldmann C. High-load nanoparticles with a chemotherapeutic SN-38/FdUMP drug cocktail. *Nanoscale*. 2024;16(31): 14853–14860. https://doi.org/10.1039/d4nr01403k.
5. Wang F, Yu L, Monopoli MP, Sandin P, Mahon E, Salvati A, et al. The biomolecular corona is retained during nanoparticle uptake and protects the cells from the damage induced by cationic nanoparticles until degraded in the lysosomes. *Nanomedicine*. 2013;9(8):1159–1168. https://doi.org/10.1016/j.nano.2013.04.010.

6. Lane R, Wolters AHG, Giepmans BNG, Hoogenboom JP. Integrated Array tomography for 3D correlative light and Electron microscopy. *Front Mol Biosci*. 2021; 8, 822232. https://doi.org/10.3389/fmolb.2021.822232.
7. Prabhakar N, Belevich I, Peurla M, Heiligenstein X, Chang H-C, Sahlgren C, et al. Cell volume (3D) correlative microscopy facilitated by intracellular fluorescent nanodiamonds as multi-modal probes. *Nanomaterials (Basel)*. 2020;11(1). https://doi.org/10.3390/nano11010014.
8. Guerin CJ, Lippens S. Correlative light and volume electron microscopy (vCLEM): how community participation can advance developing technologies. *J Microsc*. 2021;284(2):97–102. https://doi.org/10.1111/jmi.13056.
9. Lucas MS, Guenthert M, Gasser P, Lucas F, Wepf R. Correlative 3D imaging: CLSM and FIB-SEM tomography using high-pressure frozen, freeze-substituted biological samples. *Methods Mol Biol*. 2014;1117:593–616. https://doi.org/10.1007/978-1-62703-776-1_26.
10. Peddie CJ, Genoud C, Kreshuk A, Meechan K, Micheva KD, Narayan K, et al. Volume electron microscopy. *Nat Rev Methods Primers*. 2022;2:51. https://doi.org/10.1038/s43586-022-00131-9.
11. Baena V, Conrad R, Friday P, Fitzgerald E, Kim T, Bernbaum J, et al. FIB-SEM as a volume Electron microscopy approach to study cellular architectures in SARS-CoV-2 and other viral infections: a practical primer for a virologist. *Viruses*. 2021;13(4). https://doi.org/10.3390/v13040611.
12. Giepmans BNG, Deerinck TJ, Smarr BL, Jones YZ, Ellisman MH. Correlated light and electron microscopic imaging of multiple endogenous proteins using quantum dots. *Nat Methods*. 2005;2(10):743–749. https://doi.org/10.1038/nmeth791.
13. Tanner H, Sherwin O, Verkade P. Labelling strategies for correlative light electron microscopy. *Microsc Res Tech*. 2023;86(8):901–910. https://doi.org/10.1002/jemt.24304.
14. Scher N, Rechav K, Paul-Gilloteaux P, Avinoam O. In situ fiducial markers for 3D correlative cryo-fluorescence and FIB-SEM imaging. *iScience*. 2021;24(7), 102714. https://doi.org/10.1016/j.isci.2021.102714.
15. Rejman J, Oberle V, Zuhorn IS, Hoekstra D. Size-dependent internalization of particles via the pathways of clathrin- and caveolae-mediated endocytosis. *Biochem J*. 2004;377(Pt 1):159–169. https://doi.org/10.1042/BJ20031253.
16. Sahay G, Alakhova DY, Kabanov AV. Endocytosis of nanomedicines. *J Control Release*. 2010;145(3):182–195. https://doi.org/10.1016/j.jconrel.2010.01.036.
17. Kim J, Piao Y, Hyeon T. Multifunctional nanostructured materials for multimodal imaging, and simultaneous imaging and therapy. *Chem Soc Rev*. 2009;38(2): 372–390. https://doi.org/10.1039/b709883a.
18. Torchilin VP. Multifunctional nanocarriers. *Adv Drug Deliv Rev*. 2006;58(14): 1532–1555. https://doi.org/10.1016/j.addr.2006.09.009.
19. Drasler B, Vanhecke D, Rodriguez-Lorenzo L, Petri-Fink A, Rothen-Rutishauser B. Quantifying nanoparticle cellular uptake: which method is best? *Nanomedicine (London)*. 2017;12(10):1095–1099. https://doi.org/10.2217/nnm-2017-0071.
20. Pope I, Tanner H, Masia F, Payne L, Arkill KP, Mantell J, et al. Correlative light-electron microscopy using small gold nanoparticles as single probes. *Light Sci Appl*. 2023;12(1):80. https://doi.org/10.1038/s41377-023-01115-4.
21. Karreman MA, Mercier L, Schieber NL, Solecki G, Allio G, Winkler F, et al. Fast and precise targeting of single tumor cells in vivo by multimodal correlative microscopy. *J Cell Sci*. 2016;129(2):444–456. https://doi.org/10.1242/jcs.181842.
22. Sonomura T, Furuta T, Nakatani I, Yamamoto Y, Unzai T, Matsuda W, et al. Correlative analysis of immunoreactivity in confocal laser-scanning microscopy and scanning electron microscopy with focused ion beam milling. *Front Neural Circuits*. 2013;7, 26. https://doi.org/10.3389/fncir.2013.00026.
23. Schroeder-Reiter E, Pérez-Willard F, Zeile U, Wanner G. Focused ion beam (FIB) combined with high resolution scanning electron microscopy: a promising tool for 3D analysis of chromosome architecture. *J Struct Biol*. 2009;165(2):97–106. https://doi.org/10.1016/j.jsb.2008.10.002.
24. Maenz C, Lenfert E, Pantel K, Schumacher U, Deppert W, Wegwitz F. Epithelial-mesenchymal plasticity is a decisive feature for the metastatic outgrowth of disseminated WAP-T mouse mammary carcinoma cells. *BMC Cancer*. 2015;15:178. https://doi.org/10.1186/s12885-015-1165-5.
25. Schindelin J, Arganda-Carreras I, Frise E, Kaynig V, Longair M, Pietzsch T, et al. Fiji: an open-source platform for biological-image analysis. *Nat Methods*. 2012;9(7): 676–682. https://doi.org/10.1038/nmeth.2019.
26.. Marstal K, Berendsen F, Staring M, Klein S. SimpleElastix: A User-Friendly, Multi-lingual Library for Medical Image Registration. In: p. 574–582.
27. Hennies J, Lleti JMS, Schieber NL, Templin RM, Steyer AM, Schwab Y. AMST: alignment to median smoothed template for focused ion beam scanning Electron microscopy image stacks. *Sci Rep*. 2020;10(1):2004. https://doi.org/10.1038/s41598-020-58736-7.
28. Stirling DR, Swain-Bowden MJ, Lucas AM, Carpenter AE, Cimini BA, Goodman A. Cellprofiler 4: improvements in speed, utility and usability. *BMC Bioinformatics*. 2021;22(1), 433. https://doi.org/10.1186/s12859-021-04344-9.
29. Mazumdar S, Chitkara D, Mittal A. Exploration and insights into the cellular internalization and intracellular fate of amphiphilic polymeric nanocarriers. *Acta Pharm Sin B*. 2021;11(4):903–924. https://doi.org/10.1016/j.apsb.2021.02.019.
30. Sousa de Almeida M, Susnik E, Drasler B, Taladriz-Blanco P, Petri-Fink A, Rothen-Rutishauser B. Understanding nanoparticle endocytosis to improve targeting strategies in nanomedicine. *Chem Soc Rev*. 2021;50(9):5397–5434. https://doi.org/10.1039/d0cs01127d.
31. O'Connor S, Rogers D, Kobylynska M, Geraets J, Thaysen K, Egebjerg JM, et al. *Demonstrating soft X-ray tomography in the lab for correlative cryogenic biological imaging using X-rays and light microscopy*. 2024.
32. Nešić N, Heiligenstein X, Zopf L, Blüml V, Keuenhof KS, Wagner M, et al. Automated segmentation of cell organelles in volume electron microscopy using deep learning. *Microsc Res Tech*. 2024;87(8):1718–1732. https://doi.org/10.1002/jemt.24548.
33. Walter A, Kleywegt GJ, Verkade P. Correlative multimodal imaging: Building a community. *Methods Cell Biol*. 2021;162:417–430. https://doi.org/10.1016/bs.mcb.2020.12.010.